Journal of
Marine Science and Engineering

Article

Three-Dimensional Ultrasonic Reverse-Time Migration Imaging of Submarine Pipeline Nondestructive Testing in Cylindrical Coordinates

Daicheng Peng [1], Fei Cheng [2,*], Xiaoyu She [1], Yunpeng Zheng [3], Yongjie Tang [4] and Zhuo Fan [3]

[1] Key Laboratory of Exploration Technologies for Oil and Gas Resource, Ministry of Education, Yangtze University, Wuhan 430100, China; pengdc_geo@126.com (D.P.); shexiaoyu2000@163.com (X.S.)
[2] College of Marine Science and Technology, China University of Geosciences, Wuhan 430074, China
[3] Hubei Subsurface Multi-Scale Imaging Key Laboratory, School of Geophysics and Geomatics, China University of Geosciences, Wuhan 430074, China; zhengyp@cug.edu.cn (Y.Z.); zhuo@cug.edu.cn (Z.F.)
[4] Department of Earth and Space Sciences, Southern University of Science and Technology, Shenzhen 518055, China; tyj_cug@126.com
* Correspondence: chengfly03@126.com; Tel.: +86-027-67886167

Abstract: Submarine pipelines are a safe and energy-efficient mode of gas transport. However, due to the complex manufacturing process and harsh operating environment, submarine pipelines are subject to fatigue cracks under long-term cyclic loading. A comprehensive and high-precision characterization strategy for submarine pipelines can effectively prevent potential safety hazards and have significant economic and social repercussions. As a matter of fact, pipeline defects cannot be reliably detected with current traditional 2D methods. On the other hand, in ultrasonic testing, cylindrical geometry increases the complexity of the 3D wave field in the submarine pipeline space and significantly influences the accuracy of the detection results. In this paper, we put forward a novel method for 3D ultrasonic image testing that is suitable for cylindrical coordinates. In order to accurately simulate the ultrasonic signal received from pipelines, we generalize the 3D staggered-grid finite-difference method from Cartesian coordinates to cylindrical ones and simulate the full wave field in the 3D pipeline space. Then, signal processing is performed on the ultrasound simulation records, and 3D reverse-time migration imaging of submarine pipeline defects can be effectively achieved using the reverse-time migration method and cross-correlation imaging conditions. The results obtained from simulations and real field data show that the proposed method provides high-quality 3D imaging of defects in pipelines, taking into account multiple scattering and mode conversion information at the bottom of the defects.

Keywords: submarine pipelines; nondestructive testing; 3D ultrasonic imaging; reverse-time migration; cylindrical coordinates

check for updates

Citation: Peng, D.; Cheng, F.; She, X.; Zheng, Y.; Tang, Y.; Fan, Z. Three-Dimensional Ultrasonic Reverse-Time Migration Imaging of Submarine Pipeline Nondestructive Testing in Cylindrical Coordinates. *J. Mar. Sci. Eng.* **2023**, *11*, 1459. https://doi.org/10.3390/jmse11071459

Academic Editor: Sergei Chernyi

Received: 14 June 2023
Revised: 11 July 2023
Accepted: 20 July 2023
Published: 22 July 2023

1. Introduction

Submarine pipelines can connect subsea oil and gas resources with the entire onshore oil and gas production management system by the fastest, safest, and most economical route, which is called the "lifeline" of offshore oil and gas engineering [1]. However, due to the complex manufacturing processes and severe service environments [2], submarine pipelines are prone to crack voids, inclusions, and other defects, which greatly affects their mechanical properties and results in their premature failure. In real engineering applications, the initial imperfection is always introduced onto the pipes during the manufacture and installation procedures [3]. Submarine pipelines are subjected to fatigue loading in the harsh environment of the seabed operation conditions [4]. When the pipes are subjected to external pressure, failure first occurs in the cross-section with the most severe initial defects [5]. Additionally, once a crack develops, corrosion may promote its propagation, resulting in the cracking of the submarine pipeline [6]. When the pipeline is damaged and leakage occurs, it will not only cause economic losses, but also may bring about safety problems, endangering the safety of both people and the marine environment [7]. Therefore, before the submarine pipelines are put into service, a comprehensive high-precision inspection of them, including the rapid and accurate detection of defects, may effectively prevent safety hazards, which would guarantee a beneficial economic and social effect [8].

Several methods are available to inspect pipelines, including magnetic particle testing [9], magnetic flux leakage testing [10], acoustic wave testing [11], and penetration testing [12]. Ultrasonic testing may be used to detect the structure and shape of internal defects in submarine pipelines due to its high sensitivity, light equipment, and because it poses no harm to humans or the environment [13]. Ultrasonic testing can effectively detect the flaw size, the crack location [14], the elastic properties of materials [15], and the layup stacking sequence of composite materials [16,17] through the propagation of surface waves, guided waves, and body waves [18]. Then, by using ultrasonic imaging methods, defects in submarine pipelines can be visualized in an intuitive way [19–21]. The traditional ultrasonic methods of pipeline inspection include the synthetic aperture focusing technique (SAFT) [22–24], time-of-flight diffraction (TOFD) [25–27], and the total focusing method (TFM) [28,29]. Those methods have their own advantages and disadvantages. The SAFT is able to quickly provide media images; however, it has limitations in detecting vertical interfaces, lower boundaries of defects, and structures involving high-impedance contrasts. Additionally, there may be artifacts in SAFT-generated images due to surface waves, multiple reflections, and the mode conversions of the wave field originating at interfaces, resulting in wrong conclusions about the defect's location [30]. The TFM, on the other hand, only considers the direct ray path of ultrasound, without considering the mode conversions and multiple scattering arising from the interaction of ultrasonic waves with defects, which reduces the accuracy of the image [31,32]. Moreover, multiple wave reflections from the pipeline's lower side make the signals more complicated to analyze and lower the signal-to-noise ratio, often leading to artifacts in the reconstruction. As a consequence, it is difficult to image structures with vertical boundaries or complex geometry [33,34]. In order to circumvent such difficulties, modern ultrasonic testing techniques often involve full acoustic or elastic wave-equation modeling. In this paper, we address the 3D ultrasonic imaging of a pipeline using the reverse-time migration (RTM) technique, which has received much attention in the field of geophysics [35–39]. In recent years, RTM methods, originating from seismic imaging, have gained popularity in ultrasonic nondestructive testing applications [40–43]. The RTM method is a pre-stack imaging technique based on full-wave extrapolation. It does not suffer from the presence of oblique structures and offers a high resolution for the imaging of complex structures. In contrast to ray-based methods, RTM includes the effects of multiple scattering and mode conversions, as well as multiple wave reflections from the defect's lower side [33]. This allows one to gain more information, enabling the imaging of vertical interfaces and boundaries and providing higher quality images of interior defects [41,42]. However, most RTM studies on submarine pipelines are conducted using Cartesian coordinates [41,44], whereas, in any realistic case, the pipeline has an irregular cavity shape. In particular, for cylindrical structures, the pipeline's walls should be approximated as a staircase boundary using 3D Cartesian coordinates. Thus, it cannot accurately delineate the pipeline cavity, and the resulting grid scattering and dispersion analysis is affected by artifacts that reduce the imaging accuracy. To avoid those unwanted effects, we use cylindrical coordinates to model submarine pipelines in ultrasonic testing, which are more suitable for discretizing grids, and thus ensure higher accuracy [45]. In particular, using cylindrical coordinates makes the subdivision grids suitable to accurately represent the submarine pipeline cavity structure [46–48].

To address the shortcomings of traditional 2D methods and improve the accuracy of the ultrasonic characterization of submarine pipelines, we propose a 3D ultrasonic simulation and RTM imaging of submarine pipelines based on cylindrical coordinates. In our approach, the simulation of the 3D ultrasonic wave field and the wave field characteristic analysis of the submarine pipeline is performed by setting up a double free-surface and absorption boundary. Then, the ultrasonic RTM method is used to achieve high-quality 3D imaging of defects in pipelines. Numerical examples and real field data are used to prove the reliability and effectiveness of our method, paving the way for potential applications in practical ultrasonic testing.

2. Methodology

To perform accurate numerical simulations of ultrasonic waves in a 3D pipeline, we have developed a variable staggered-grid time-domain finite-difference numerical simulation method (FDM) in cylindrical coordinates. In the following paragraphs, we provide a brief description of the elastic wave equation, grid discretization, and boundary conditions in cylindrical coordinates.

2.1. Equations of Motion and Grid Discretization in Cylindrical Coordinates

For isotropic media, the first-order velocity-stress equation in the cylindrical coordinates (r, θ, z) can be expressed as follows [49]:

$$\begin{cases} \rho \frac{\partial v_r}{\partial t} = \frac{\partial \sigma_{rr}}{\partial r} + \frac{1}{r}\frac{\partial \tau_{r\theta}}{\partial \theta} + \frac{\partial \tau_{rz}}{\partial z} + \frac{\sigma_{rr}-\sigma_{\theta\theta}}{r} + f_r \\ \rho \frac{\partial v_\theta}{\partial t} = \frac{\partial \tau_{r\theta}}{\partial r} + \frac{1}{r}\frac{\partial \sigma_{\theta\theta}}{\partial \theta} + \frac{\partial \tau_{\theta z}}{\partial z} + \frac{2\tau_{r\theta}}{r} + f_\theta \\ \rho \frac{\partial v_z}{\partial t} = \frac{\partial \tau_{rz}}{\partial r} + \frac{1}{r}\frac{\partial \tau_{\theta z}}{\partial \theta} + \frac{\partial \sigma_{zz}}{\partial z} + \frac{2\tau_{rz}}{r} + f_z \end{cases} \tag{1}$$

$$\begin{cases} \frac{\partial \sigma_{rr}}{\partial t} = (\lambda + 2\mu)\frac{\partial v_r}{\partial r} + \lambda \frac{v_r}{r} + \frac{\lambda}{r}\frac{\partial v_\theta}{\partial \theta} + \lambda \frac{\partial v_z}{\partial z} + g_{rr} \\ \frac{\partial \sigma_{\theta\theta}}{\partial t} = \lambda \frac{\partial v_r}{\partial r} + (\lambda + 2\mu)\left(\frac{v_r}{r} + \frac{1}{r}\frac{\partial v_\theta}{\partial \theta}\right) + \lambda \frac{\partial v_z}{\partial z} + g_{\theta\theta} \\ \frac{\partial \sigma_{zz}}{\partial t} = \lambda \frac{\partial v_r}{\partial r} + \lambda\left(\frac{v_r}{r} + \frac{1}{r}\frac{\partial v_\theta}{\partial \theta}\right) + (\lambda + 2\mu)\frac{\partial v_z}{\partial z} + g_{zz} \\ \frac{\partial \tau_{r\theta}}{\partial t} = \mu\left(\frac{1}{r}\frac{\partial v_r}{\partial \theta} - \frac{v_\theta}{r} + \frac{\partial v_\theta}{\partial r}\right) + g_{r\theta} \\ \frac{\partial \tau_{rz}}{\partial t} = \mu\left(\frac{\partial v_r}{\partial z} + \frac{\partial v_z}{\partial r}\right) + g_{rz} \\ \frac{\partial \tau_{\theta z}}{\partial t} = \mu\left(\frac{\partial v_\theta}{\partial z} + \frac{1}{r}\frac{\partial v_z}{\partial \theta}\right) + g_{\theta z} \end{cases} \tag{2}$$

where $f_i(i = r, \theta, z)$ denotes the point force source, $g_{ij}(i, j = r, \theta, z)$ represents the coupling, ρ represents the density, λ and μ are the Lame constants, $v_i(i = r, \theta, z)$ denotes the particle velocity in the i direction, $\sigma_{ii}(i = r, \theta, z)$ is the normal stress, and $\tau_{ij}(i, j = r, \theta, z)$ denotes the shear stress. Simulations of the wave field in time-domain FDM may be implemented by discretizing Equations (1) and (2) using a central differencing scheme with a staggered grid both in spatial and temporal domains [50]. As shown in Figure 1, within cell (i, j, k), the normal stresses $\sigma_{ii}(i = r, \theta, z)$ are located on the nodes (i, j, k), the shear stresses $\tau_{ij}(i, j = r, \theta, z)$ are located on the half nodes $(i + 1/2, j, k + 1/2)$, $(i, j + 1/2, k + 1/2)$, and $(i + 1/2, j + 1/2, k)$, and the velocity components $v_i(i = r, \theta, z)$ are located on the half nodes $(i + 1/2, j, k)$, $(i, j + 1/2, k)$, and $(i, j, k + 1/2)$. Then, according to the staggered grid with discretized points of velocity and stress components in Figure 1, Equations (1) and (2) are dissected in a finite-difference staggered-grid scheme. More details of the 3D time-domain FDM can be found in Liu et al. [49] for cylindrical coordinates.

2.2. Boundary Conditions

In finite-difference forward modeling of submarine pipelines, the boundary conditions are particularly important to properly simulate the propagation of ultrasonic waves. Figure 2 illustrates a schematic diagram of the implementation of boundary conditions. The absorbing boundary is placed along the R- and Z-direction of the model area, while the double free-surface boundary is along the inner and outer θ-direction of the pipeline. In our study, for the sake of computational efficiency, we introduce an improved vacuum formulation [51] into the cylindrical coordinates to set the double free-surface boundary condition in the θ-direction. At variance with the acoustic-elastic boundary method, which requires setting the free-surface boundary condition individually for each case, the improved vacuum formulation (IVF) is adaptable to an irregular free-surface. In order to eliminate interference from the region outside of the model, an absorbing boundary condition is assumed on the exterior of the model. We employ the split-field perfectly matched layer (S-PML) [52] to optimize absorption and minimize computational costs. As shown in Figure 2, the S-PML is placed in the *R*-direction and *Z*-direction of the pipe to absorb the body waves propagating toward the model boundary. The attenuation factor d(x_{i}) of the absorbing boundaries is given by the following expression:

$$d(x_i) = \log\left(\frac{1}{R}\right)\frac{3V_p^{\max}}{2L}\left(\frac{x_i}{L}\right)^2 (i = r, z) \tag{3}$$

where R is the theoretical reflection coefficient, L is the thickness of the absorbing boundary, and x_i is the distance between grid points and model boundaries in the i direction.

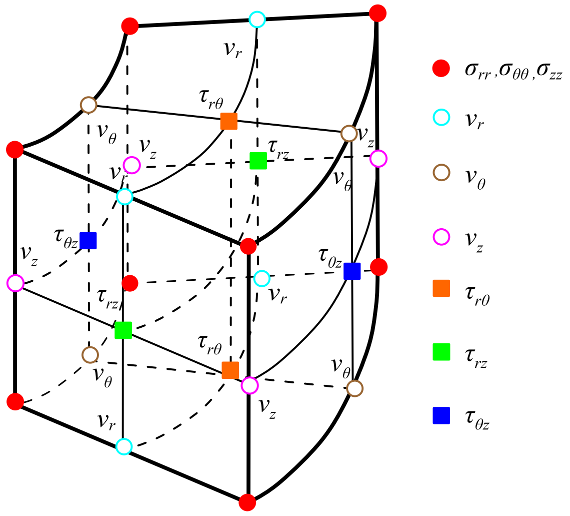

Figure 1. Staggered grid with discretized points of velocity and stress components. The $\sigma_{rr}, \sigma_{\theta\theta}, \sigma_{zz}$ denote the normal stresses, v_r, v_θ, v_z are the particle velocity components, and $\tau_{r\theta}, \tau_{rz}, \tau_{\theta z}$ represent the shear stresses. The normal stresses are placed at the corner points around the staggered-grid cell, the particle velocity components are located at the cell edges, and the shear stresses are sampled at the center of the cell faces.

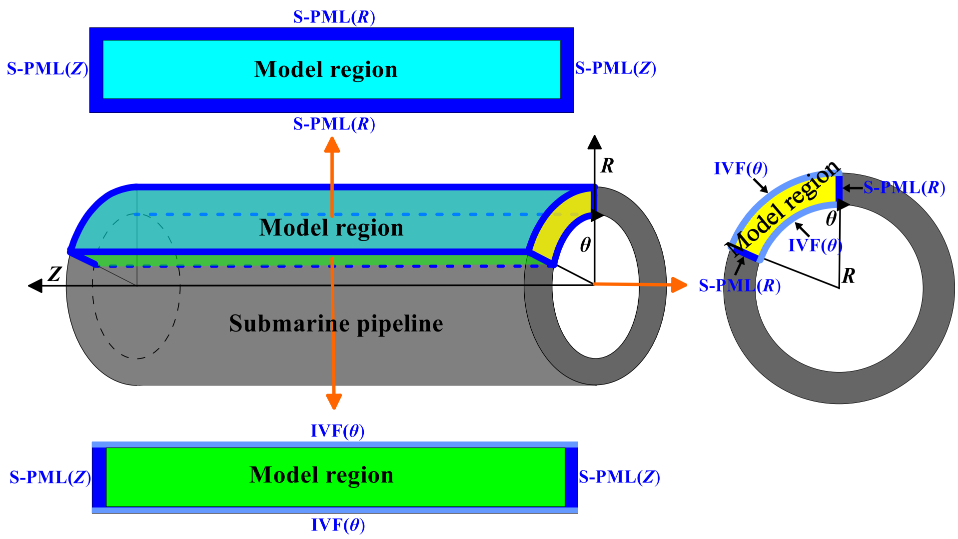

Figure 2. Schematic diagram of the model, illustrating the implementation of the boundary conditions. The absorbing boundary (S-PML) is placed along the *R*- and *Z*-direction of the model region, and the double free-surface boundary (IVF) is along the inner and outer *θ*-direction of the model region.

2.3. Reverse-Time Migration Method

Reverse-time migration (RTM), originally proposed by Whitemore, is based on the two-way wave equation, on which reverse-time extrapolation is performed on the time axis [35]. RTM was first applied to the field of seismic imaging, providing higher imaging accuracy than previous methods. Besides accuracy, RTM has no inclination limitation and may be applied to arbitrary complex velocity models [36,37]. The RTM algorithm consists of the following three steps: 1. forward propagation of the source wave fields; 2. backward propagation of the receiving wave fields; and 3. imaging using imaging conditions. In this study, we used cross-correlation imaging conditions, followed by source normalization, ultimately leading to the following expression [53]:

$$I(r,\theta,z) = \frac{\sum_{t=0}^{T} S(r,\theta,z,t)R(r,\theta,z,t)}{\sum_{t=0}^{T} S^2(r,\theta,z,t)} \tag{4}$$

where $I(r,\theta,z)$ represents the image result, $S(r,\theta,z,t)$ denotes the source field, and $R(r,\theta,z,t)$ is the field at the receiver. After that, the Laplace filtering method is employed to eliminate the low-frequency artifacts caused by the imaging conditions [54].

2.4. Signal Processing

The wavefields obtained from pipeline ultrasound inspection records are characterized by complex features, such that the preprocessing of records is required before imaging to enhance RTM accuracy. In this study, wavelet extraction and dynamic balance in the channel are employed. Wavelet extraction methods may be classified into two categories: deterministic [55] and statistical [56]. In this study, the statistical wavelet extraction method is employed to extract wavelets from reflected waves. To this aim, we have to first select the reference trace, and then search for wavelets of other tracks within the travel time range of the reflected wave using this reference track as a guide. Finally, we normalize the wavelets of all traces, and then stack all traces in the record.

2.5. Implementations

Figure 3 illustrates the steps of the proposed method. The first step is to construct a geophysical 3D submarine pipeline model and implement the staggered-grid finite-difference method in cylindrical coordinates. Then, the SPML-absorbing and the IVF double free-surface boundary conditions are implemented in cylindrical coordinates and a 3D ultrasonic wave field simulation of the submarine pipeline is performed. RTM calculations represent the third and final step. RTM itself involves three steps, i.e., the forward propagation of source wave fields, the backward propagation of receiver wave fields, and the imaging step using the imaging condition. The procedure is carried out as follows: At first, a source wavelet is placed on the pipeline surface and used to excite the propagation of ultrasonic waves. The source wave fields during the forward propagation from T = 0 to T = max are calculated. Then, the recorded signal at the boundaries is time-reversed and simultaneously propagated back into the simulation domain to obtain the source wave fields from T = max to T = 0. Then, signal processing is performed and used as a signal at the receiver position. The receiver wave fields are then calculated using the FDM. Finally, the source wave fields are cross correlated with the receiver wave fields at each time step to construct the image. The final ultrasonic 3D RTM imaging is obtained using Laplace filtering [54].

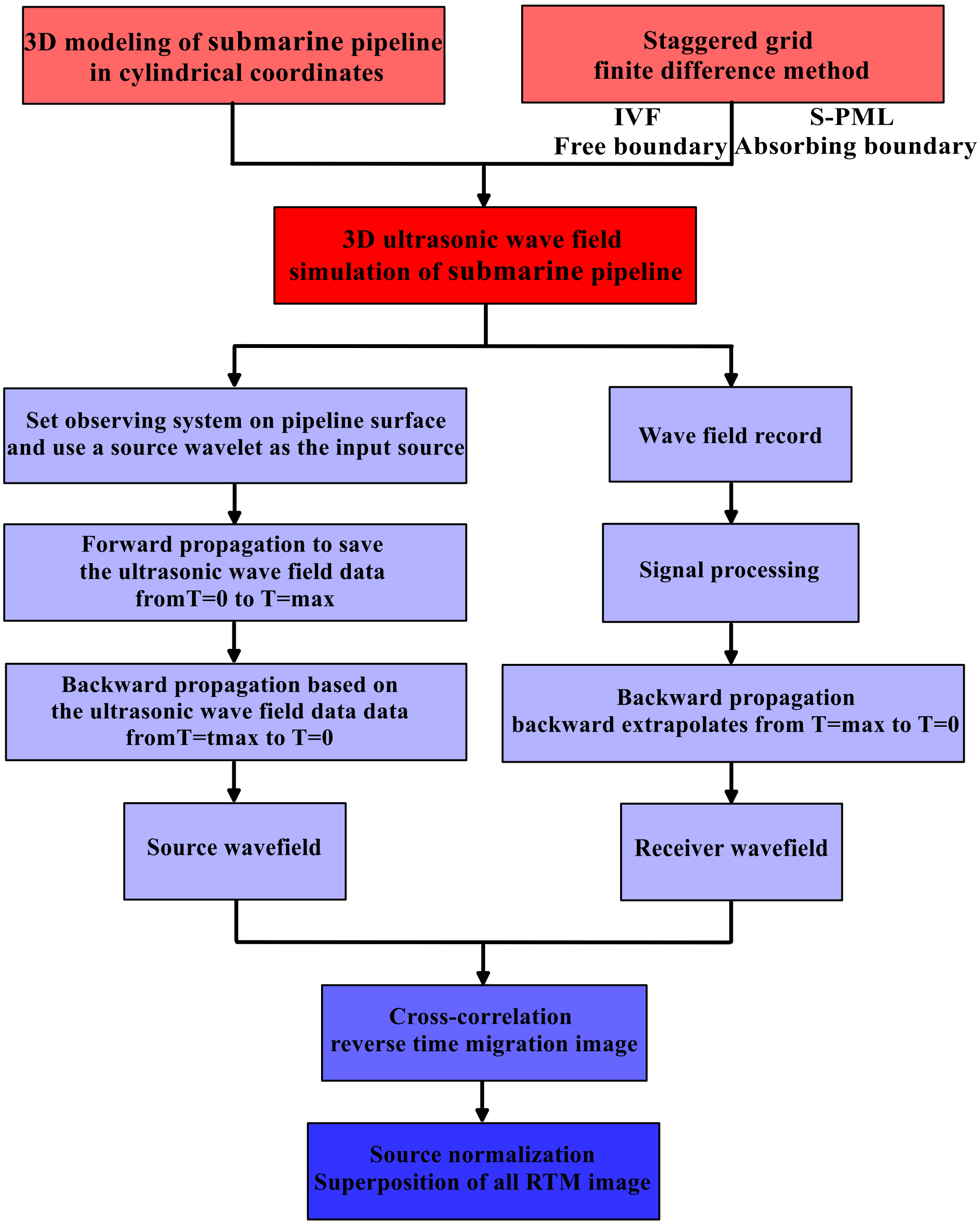

Figure 3. A flow-chart of implementation.

3. Numerical Simulation Results

3.1. Modeling and Survey Layout

3.1.1. Survey Layout

Our 3D cylindrical model of a submarine pipeline is shown in Figure 4. It includes a total of six survey lines arranged in the model region. Geophones are placed at the bottom, middle, and top of the pipeline's outer wall. The geophones are piezoelectric ceramic ultrasonic probes. Three survey lines are circumferentially placed (red lines in Figure 4), with a geophone spacing of 1.0 mm (Line-θ1, Line-θ2, and Line-θ3) and three are placed axially (blue lines in Figure 4), with a geophone spacing of 1.0 mm (Line-Z1, Line-Z2, and Line-Z3). The source is located at the center of the pipeline's outer wall.

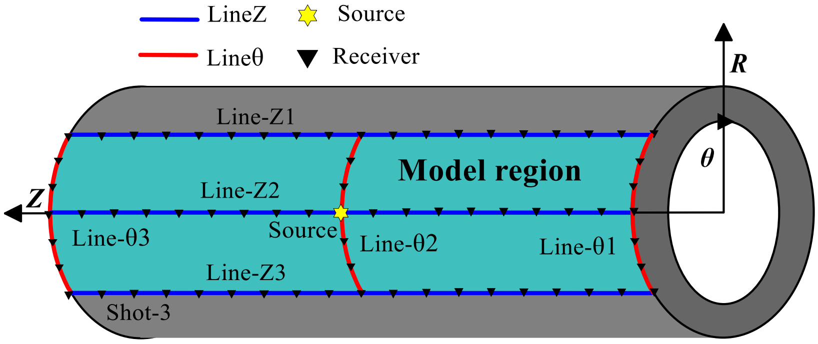

Figure 4. Schematic diagram of the ultrasonic testing and observation system.

3.1.2. Modeling

To analyze the propagation characteristics of the 3D wave field during the ultrasonic testing of pipelines, and to study the wave field characteristics resulting from different defects, we have designed three models (see Figure 5). Model-1 is a combined model of horizontal slag inclusion and hole defects, where the thickness of the slag is 2.0 mm, the width is 51.45 mm, the diameter of the hole is 2.4 mm, and the distance between the hole and the slag is 40 mm. Model-2 is a vertical slag inclusion model with a vertical thickness of 1.0 mm, a width of 51.45 mm, and a length of 60.0 mm. Model-3 describes another vertical slag inclusion with a slag width of 1.0 mm and a length of 60.0 mm. The model parameters are listed in Table 1.

Table 1. Parameters of the three models.

No.	$v_p(m/s)$	$\rho(kg/m^3)$
(1) Slag inclusion	1866.0	2466.0
(2) Hole	1400.0	1850.0
(3) Submarine pipeline	5600.0	7400.0

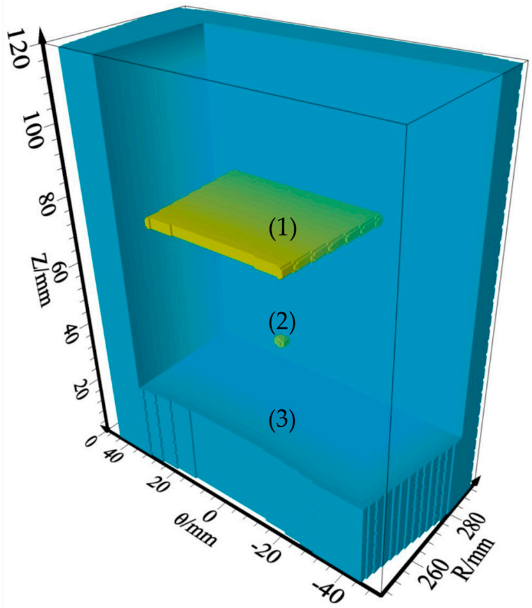

(**a**)

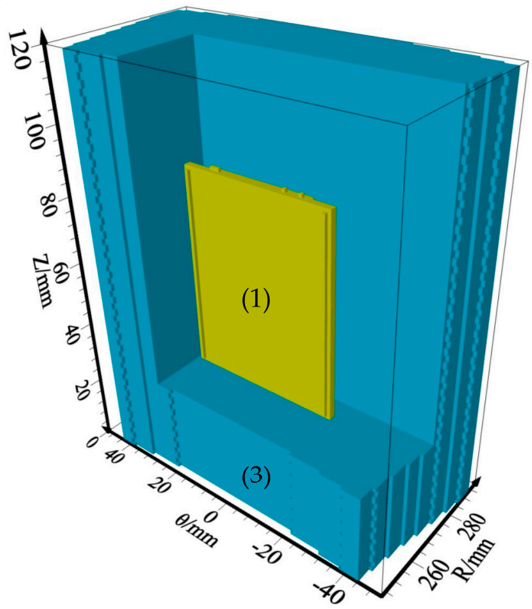

(**b**)

Figure 5. *Cont.*

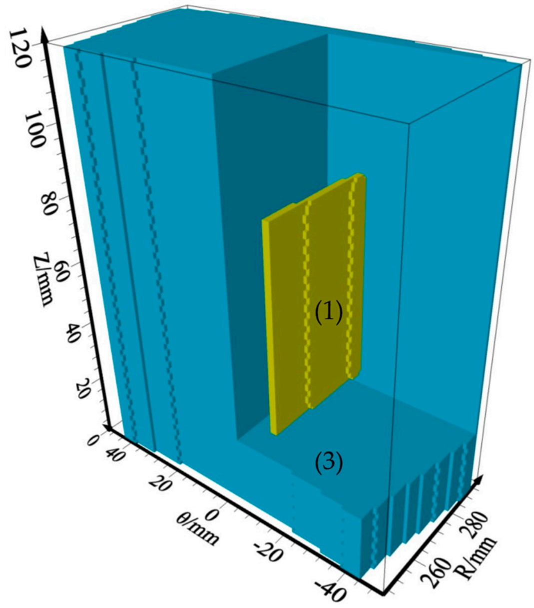

(c)

Figure 5. Submarine pipeline models developed to perform numerical simulations. (**a**) Combined model of a horizontal slag inclusion and a hole; (**b**) Vertical slag inclusion Model 1; and (**c**) Vertical slag inclusion 2. All parameters (1)–(3) in the figure are shown in Table 1.

3.2. Forward Modeling Results

In this study, we employ a spatial fourth-order and temporal second-order variable staggered-grid FDM. In our 3D cylindrical submarine pipeline model, the wall thickness is 45.0 mm, the inner diameter is 250.0 mm, the arc length is 102.97 mm (with a 20° rounding angle), and the axial length is 120.0 mm. The model size in the R-, θ-, and Z-directions is 45.0 mm × 102.97 mm (20°) × 120.0 mm. The radial step in the R-direction and the axial step in the Z-direction are $\Delta r = \Delta z = 0.2$ mm. The azimuthal step in the θ-direction is $\Delta\theta = 0.046°$. The corresponding arc length increases with the increase in wall thickness (0.2 mm at the inner wall and 0.236 mm at the outer wall). The time step of $\Delta t = 0.01$ µs. To ensure the consistency with the actual ultrasonic source, we assume a point-like force source. As shown in Figure 6, the source wavelet is a ricker wavelet with a frequency of 0.7 Mhz, a signal width of 0.33–1.16 Mhz, and a wavelet delay of 1.71 µs.

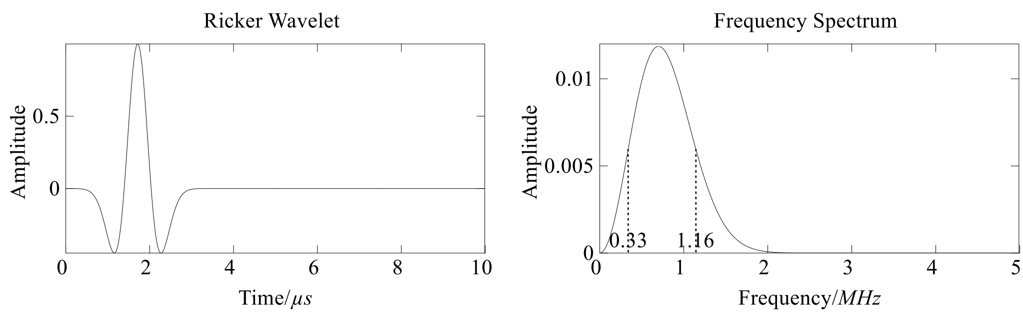

(**a**) (**b**)

Figure 6. (**a**) Ricker wavelet waveform diagram and (**b**) Ricker wavelet spectrogram.

In order to visually analyze the propagation of the wavefields in Model-1, we consider the 3D wavefield snapshots at T = 12 µs, and the 2D wavefield snapshot profiles from three slice directions at T = 6, 12, and 18 µs. Figure 7a shows the 3D wavefield snapshot, where the yellow color indicates the defect's location; Figure 7b shows a slice diagram, where green indicates a ROZ slice located at the midpoint position in the θ-direction, purple denotes a ROθ slice located at the midpoint in the Z-direction, and orange indicates a θOZ slice located at the pipeline's outer wall; and Figure 7c shows snapshots of the 2D wavefield in three slices.

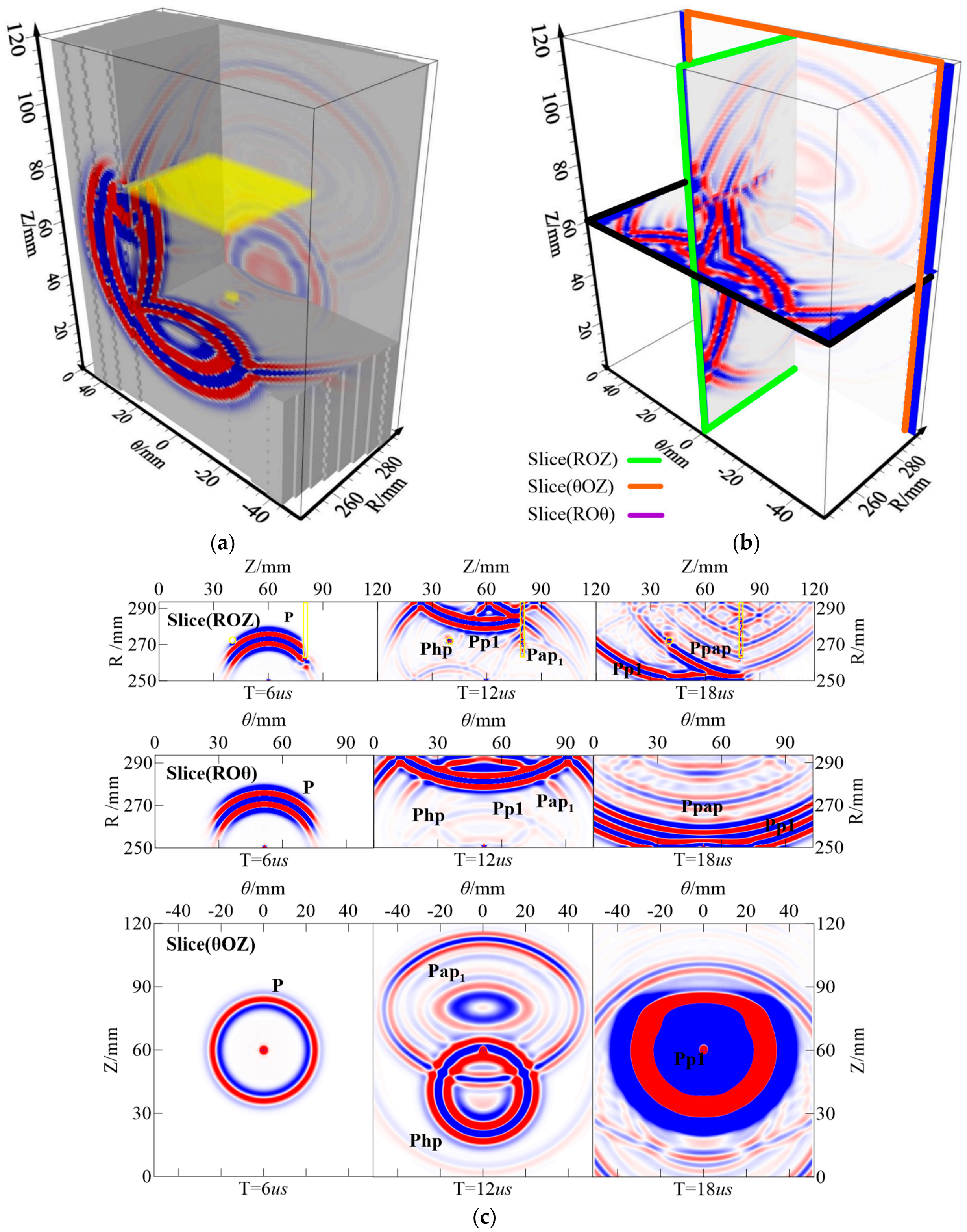

Figure 7. The radial component wave field snapshot (the yellow color indicates the defects location). (**a**) Show 3D snapshot at time T = 12 μs; (**b**) Slice diagram; and (**c**) Show 2D snapshot at time T = 6, 12, and 18 μs.

In Figure 7, at 6 μs, we only see the direct wave P, because the wavefront has not yet encountered the defect. At 12 μs, since the Fresnel condition is not satisfied, the diffraction wave Php is generated when the P wave passes through the hole. The diffraction wave Pap1 is produced when the P wave passes through the upper interface of the slag inclusion. At 18 μs, we see the reflection wave Pp1, which is generated when the P wave reaches the free-surface boundary of the pipeline's outer wall. When the reflected wave Pp1 reaches the slag inclusion defect, it generates a reflected diffracted wave Ppap. Overall, the kinematics and dynamics of each wave item are consistent with the wave field law, which confirms the accuracy of the wave field simulations.

3.2.1. Model-1

Based on the observation system in Figure 4, we were able to generate the wave field records of the two sets of survey lines through forward modeling. The simulation record of Model-1 is illustrated in Figure 8. Trace refers to the number of geophones in the survey line. As can be seen from the plots, the direct wave P, the reflected wave Pp1, the multiple Pp2, the diffraction wave Php, and the diffraction wave Pap1 carry most of the energy. Nevertheless, the diffraction waves Ppap generated by the Pp1 are also evident. According to the simulations, the arrival time of the direct wave P is 9.19 μs and the arrival times of the diffraction waves Pap1 and Php are 13.51 μs and 15.41 μs, respectively. The arrival time of the reflected wave Pp1 is 18.52 μs and the Ppap is 22.06 μs. This result confirms that the simulation results are accurate.

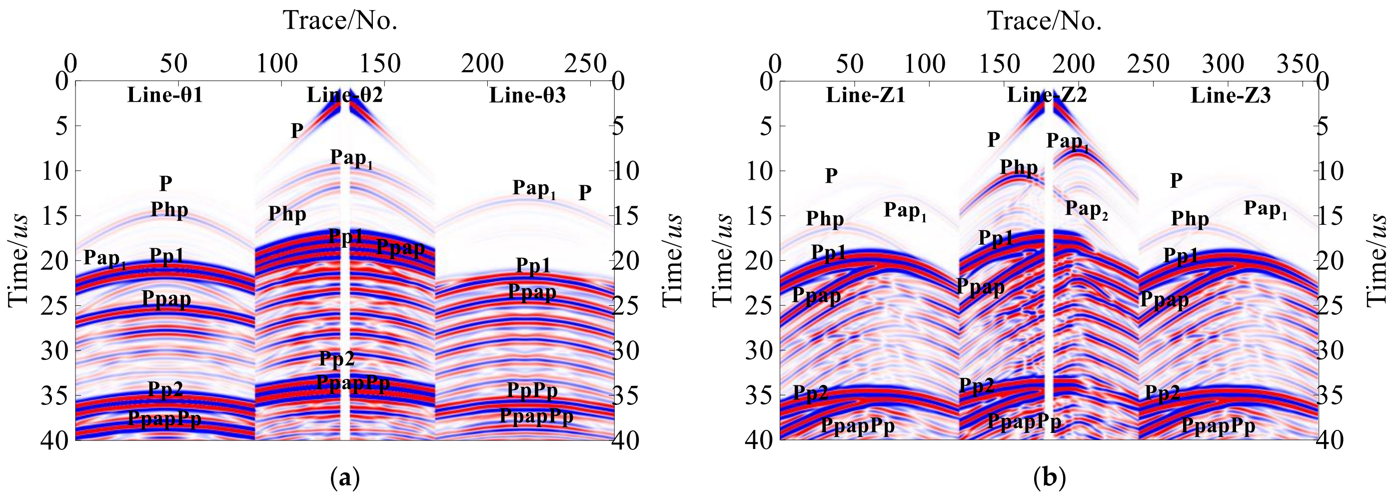

Figure 8. Synthetic *R*-component records of Model-1 (**a**) Line-θ1~θ3 and (**b**) Line-Z1~Z3.

3.2.2. Model-2

The results from Model-2 are consistent with those from Model-1. In particular, we see in Figure 9 that increasing the propagation length of the P wave leads to a reduced energy of the wave field and a corresponding reduction in the energy received by the geophone on both sides of the pipeline. Nevertheless, both the primary reflection waves Pmp and secondary reflection waves Pmp2 resulting from the vertical slag inclusion defect and the reflected waves Pmm reflected from the inner wall of the pipeline have high energy, which can be precisely identified. In addition, the diffraction waves PmD1 and PmD2 from the vertical slag defect endpoints are also clearly visible.

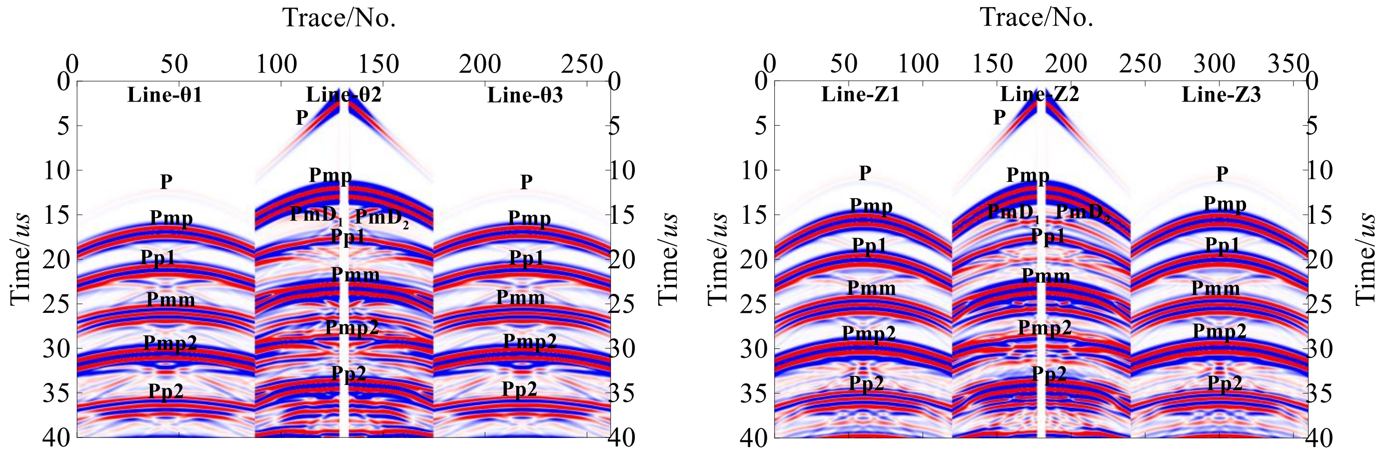

(**a**) (**b**)

Figure 9. Synthetic *R*-component records of Model-2 (**a**) Line-θ1~θ3 and (**b**) Line-Z1~Z3.

3.2.3. Model-3

In addition, the results of Model-3 are consistent with those of Model-1. We see in Figure 10 that the direct wave P and the reflected wave Pap from the vertical slag inclusion are weak in Line-θ1 and Line-θ3, while the reflected wave Pp1 and the reflected wave Ppap from the inner wall of the pipeline through the vertical slag are stronger. Nevertheless, the direct and reflected waves are clearly visible along Line-θ2, with energy decreasing with distance.

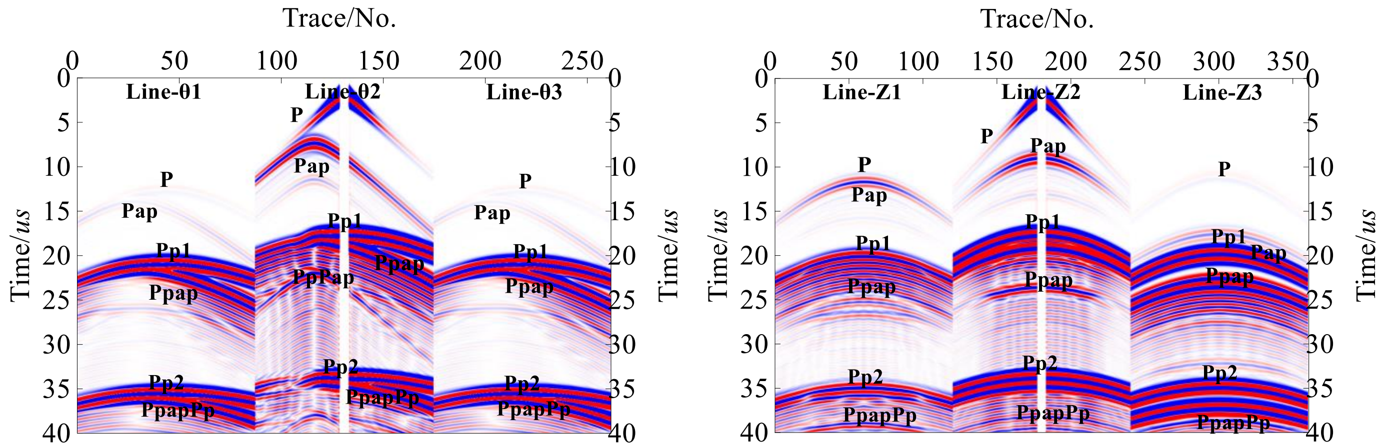

(**a**) (**b**)

Figure 10. Synthetic *R*-component records of Model-3 (**a**) Line-θ1~θ3 and (**b**) Line-Z1~Z3.

3.3. RTM Results

3.3.1. Signal Processing Results

The signal processing of wavefield records is one of the key steps in RTM imaging, and it ultimately determines the overall quality of the imaging. Here, we present the results from the signal processing of the original recordings of Model-3. Looking at Figure 10a, we can see that there is a large amount of information in the unprocessed original record, which interferes with the defect reflection wave. We thus start with removing the direct wave P (see Figure 11) and then proceed with the wavelet extraction method to suppress the free-surface boundary reflection wave. Finally, the dynamic balance in the track is used to obtain the final record, which is characterized by an improved signal-to-noise ratio.

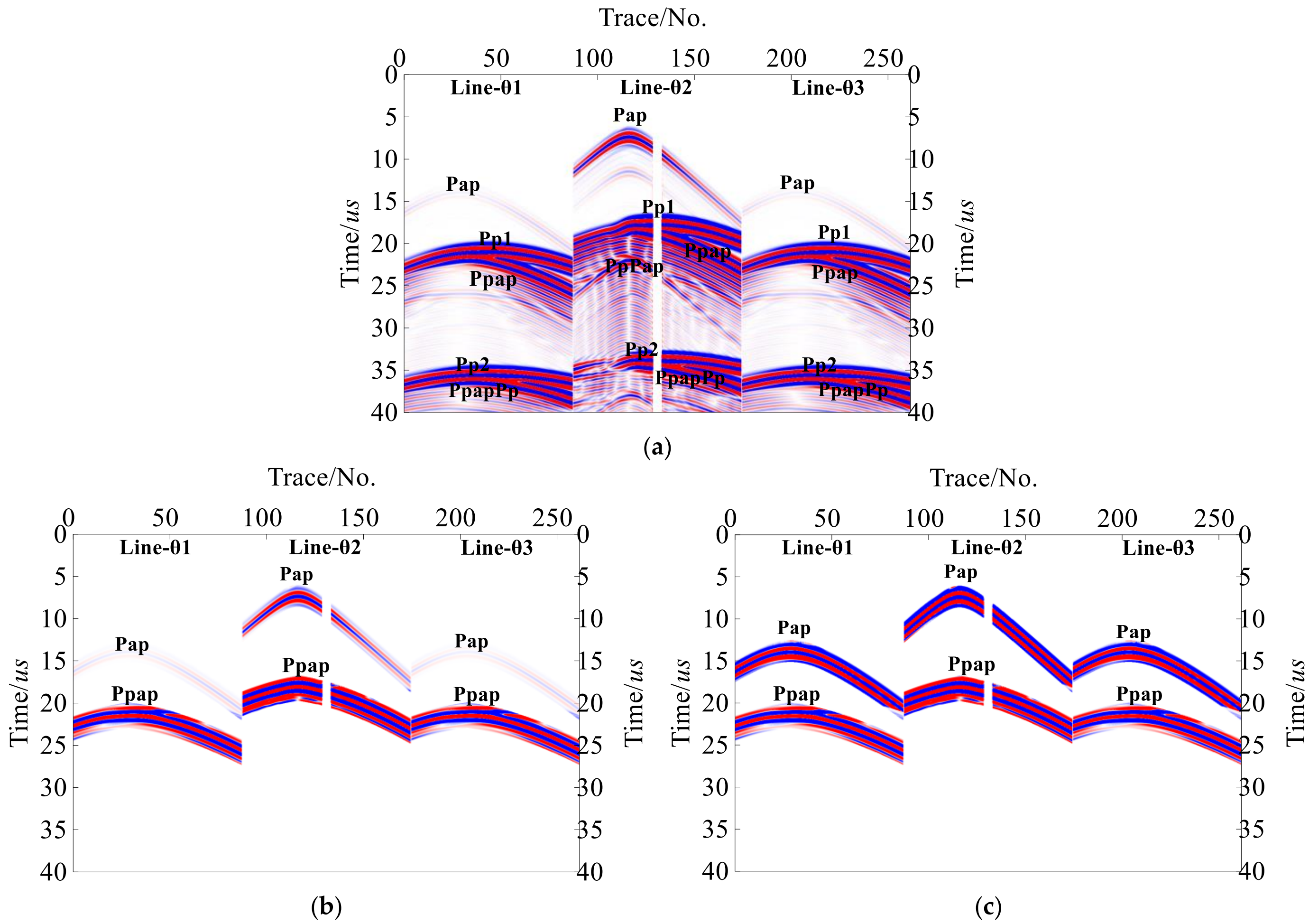

Figure 11. Signal processing results. (**a**) Record after direct wave removal; (**b**) Record after reflected wave suppression; and (**c**) Record after dynamic balance within the track.

3.3.2. Imaging Results

Figure 12 illustrates the results of RTM imaging for Model-2 after signal processing. As shown in Figure 12a, the unprocessed RTM image has a very low signal-to-noise ratio and contains many artifacts, which makes it impossible to identify the slag inclusion defect accurately. From Figure 12b, we can see that removing the direct wave allows us to eliminate the yellow-dashed-frame artifact on the outer wall of the pipeline. After the suppression of the free-surface boundary reflection wave, we obtain the image shown in Figure 12c, where the red-dotted-frame artifact has also been removed. Finally, using dynamic balance within the track, we improve the signal-to-noise ratio and obtain the final image of Figure 12d. When compared with the initial model in Figure 12a, it is evident that the position and shape of the vertical slag inclusion defect are essentially the same, and no other artifacts are present.

Figure 13 shows the three-dimensional ultrasonic RTM images obtained in cylindrical coordinates denoised with a Laplace filter and with the noise of the receiver point removed. The results for a hole defect are shown in Figure 13a, where the location and shape are clearly visible. The same is true for the boundaries and the position of the slag inclusion interface, as shown in Figure 13b. Figure 13c shows that, for a vertical slag inclusion defect, the upper and lower boundaries can be well imaged, as well as its bottom boundary. The position of the boundaries corresponds to those of the real model, and, although the lack of reflection point removes the information in the central region, the four boundaries are sufficient for determining the location of the slag inclusions.

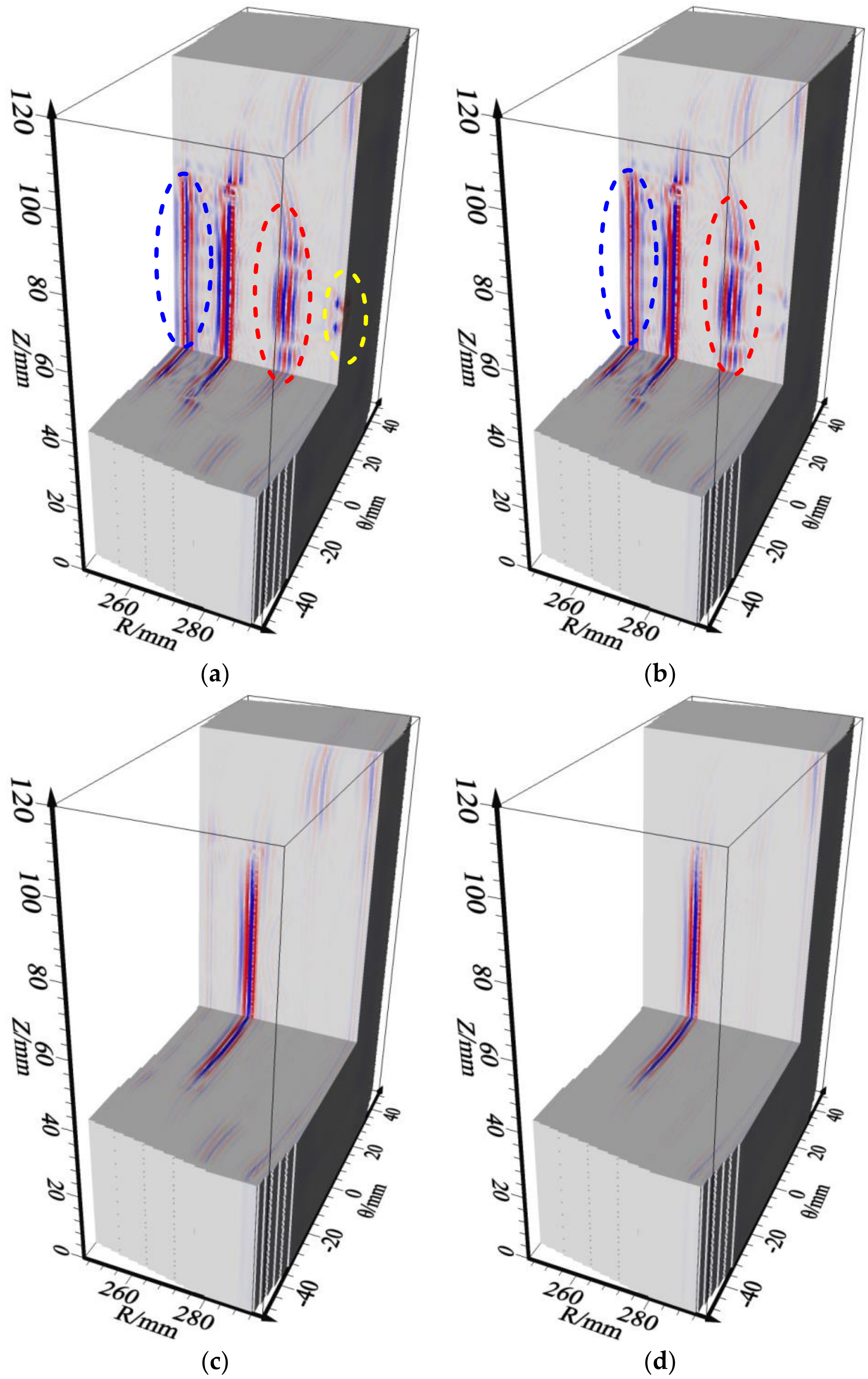

Figure 12. Imaging results: (**a**) Unprocessed imaging; (**b**) Imaging after direct wave removal; (**c**) Imaging after reflected wave suppression; and (**d**) Imaging after dynamic balance within the track.

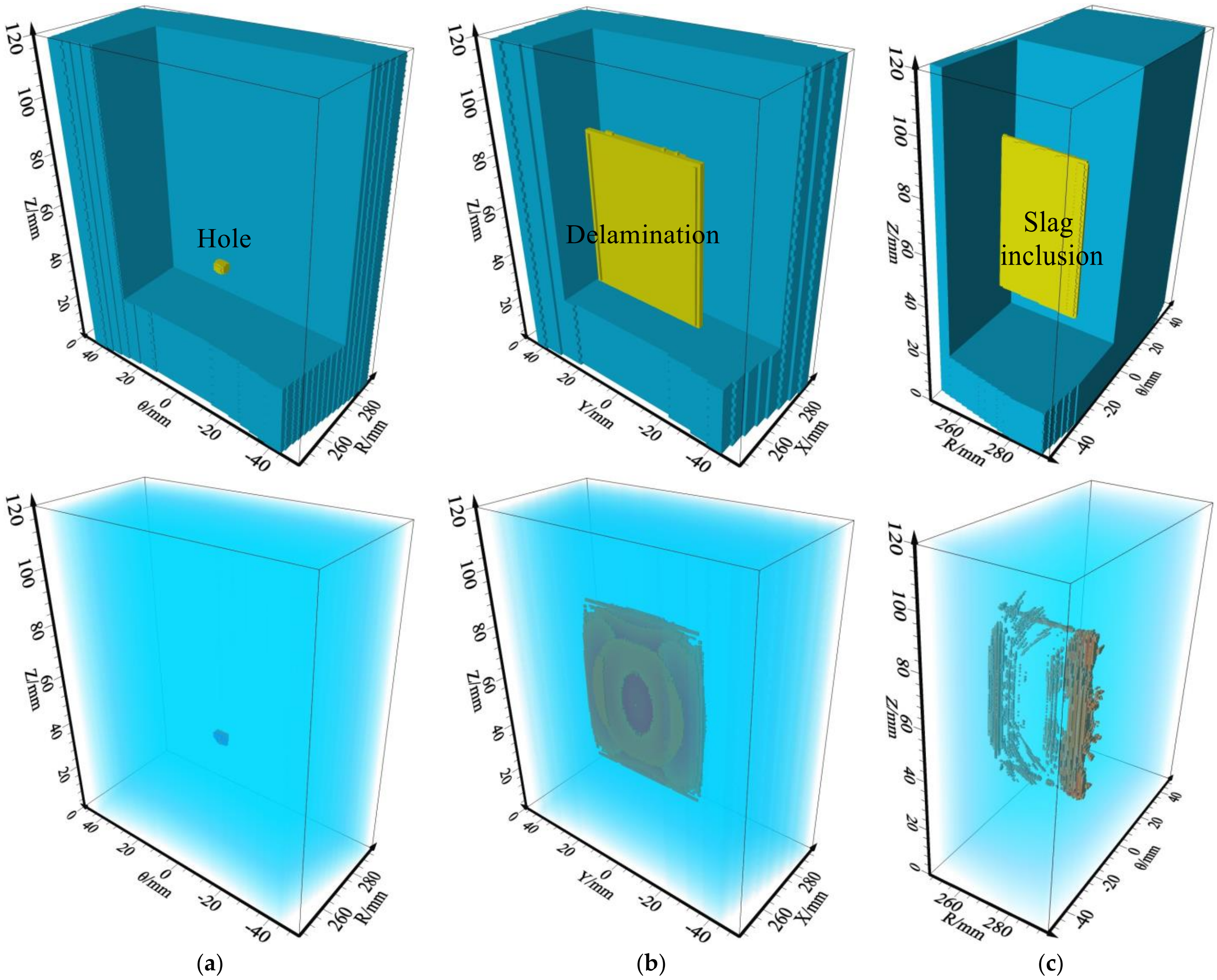

Figure 13. Three-dimensional ultrasonic RTM imaging results: (**a**) Hole defect; (**b**) Lamination defect; and (**c**) Slag inclusion.

4. Laboratory Experiment and Results

4.1. Experimental Setup and Observing System

Ultrasonic seismic physics simulation laboratory equipment is used to collect the actual data underwater for pipelines with defects. Figure 14 illustrates the major components of the data acquisition equipment. The ultrasonic data acquisition system consists of a computer, an ultrasonic pulse transmitter, a water pool, high-speed data-acquisition, and a probe-motion double-3D-coordinate automatic positioning control system. The experimental procedure is as follows: The computer sets the parameters for the sampling points, the starting and ending position of the receiver probe, and so on. Then, the 3D positioning device moves between the sampling start and end points. Once the ultrasonic receiving transducer reaches a sampling point, the ultrasonic pulse generator transmits a fixed-length synchronous signal. Finally, the ultrasonic signal received by the ultrasonic receiving transducer is sent to the computer for processing.

The experimental specimen is shown in Figure 14c. The submarine pipeline length is 550 mm, the outside diameter is 219 mm, and the wall thickness is 45 mm. In order to simulate slag inclusions in actual an ultrasonic testing, cement is injected into the crack to simulate a low velocity body. The slag inclusion on the outer wall of the pipeline measures 60 mm in arc length, 3 mm in width, and 22.5 mm in depth. As shown in Figure 14d, for this slag entrapment model, we designed an observation system on the outer wall of the pipeline, with a total of seven lines. The spacing between each line is 1 cm, the length of each line is 150 mm, the channel spacing is 1 mm, and the sampling time is 60 µs. The source is located at the end point, and the offset distance is 2 cm. The ultrasonic pulse generation receiver frequency is 0.5 MHz.

Figure 14. Ultrasonic experimental setup and observing system. (**a**) Three-dimensional positioning instrument mechanism; (**b**) Ultrasonic pulse generator; (**c**) Specimen; and (**d**) Observing system.

4.2. Results

Figure 15 illustrates the actual filtered data. The direct wave P can be clearly seen, as well as the surface wave R, and slag inclusions diffraction wave Pap. Since water is used as a coupling agent, the ultrasonic excitation propagates in the pipeline, and also in the water, thus producing a direct wave Pw, whose speed is much slower than the propagation in the steel pipe (medium speed), but with greater energy.

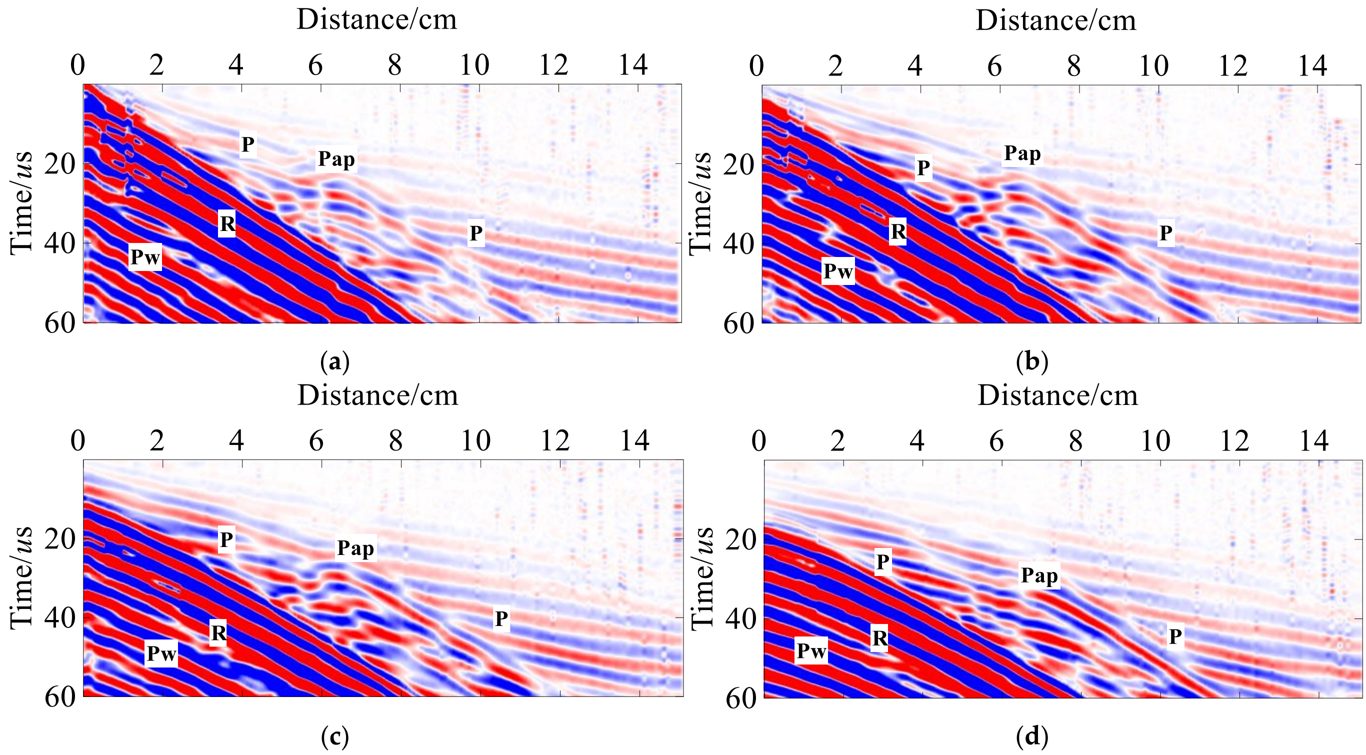

Figure 15. Ultrasonic test data. (**a**–**d**) Line-1~Line-4.

We have also constructed a pipeline model with the same slag inclusion defect, matching the size and physical parameters of the test. The simulation data (Figure 16a) are compared to the experimental data (Figure 16b). The figure illustrates that the diffracted wave Pap position of the defect is basically the same. In the experimental data, we can see the effects of t noise and absorption by the water layer, resulting in a low excitation frequency, incomplete wave field separation, and R energy covering part of the effective wave field. However, the diffraction wave Pap of the slag inclusions can still be identified, thereby confirming the reliability of our cylindrical FDM simulations in providing theoretical guidance for the ultrasonic nondestructive testing of pipeline defects.

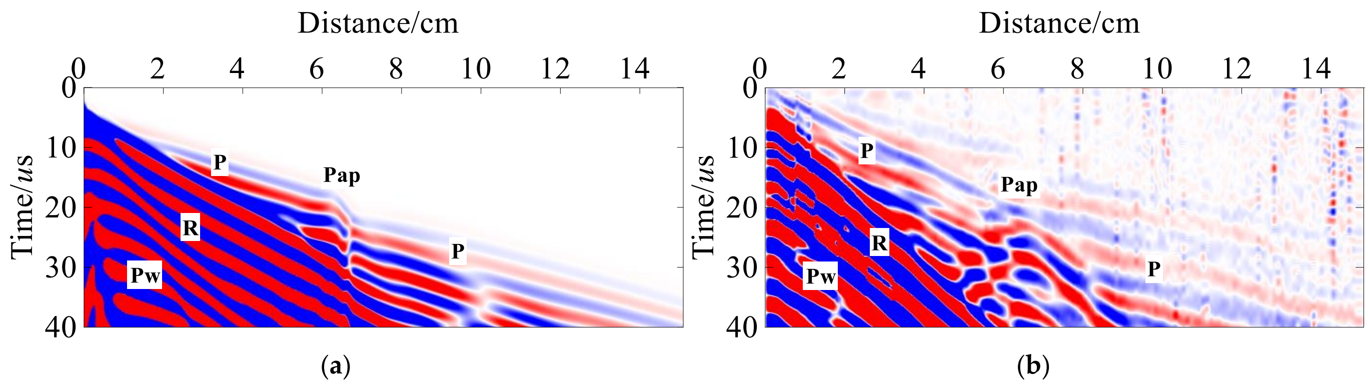

Figure 16. Comparison of test and simulation records. (**a**) Simulation record and (**b**) Test record.

Based on the actual ultrasound Line-1~Line-7 data, cross-correlation imaging conditions are used for RTM imaging after data processing. The imaging results after noise processing are shown in Figure 17b. The image clearly shows the lower interface and vertical boundaries of the defect, and the wave field energy is concentrated at the real cement-filled defects. The results confirm the reliability of the method proposed in this paper, and that ultrasonic testing of submarine pipelines is feasible.

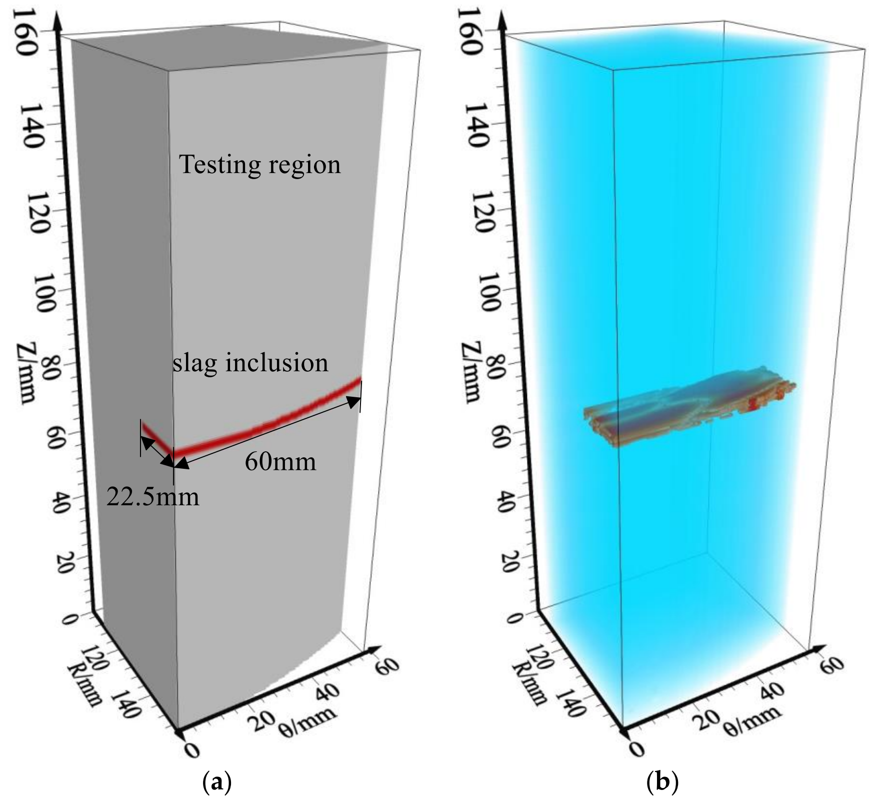

Figure 17. The test results of 3D ultrasonic RTM imaging. (**a**) Test Model and (**b**) 3D ultrasonic RTM imaging.

5. Conclusions

In this study, we have proposed a staggered-grid FDM in cylindrical coordinates to match the natural cylindrical symmetry of submarine pipeline cavities. A realistic pipeline model has been designed by including a double free-surface boundary and an absorbing boundary. Using this scheme, we have simulated the ultrasonic wave fields resulting from three types of defects in pipelines, i.e., a hole, a vertical slag inclusion defect, and a horizontal slag inclusion. Numerical and experimental examples are provided to verify the reliability and accuracy of the method. Signal processing has been performed using the ultrasonic information at hand. In particular, by using cross-correlation imaging conditions, 3D RTM imaging of a pipeline's space in cylindrical coordinates has been realized. Compared to traditional 2D ultrasonic testing methods, our scheme is capable of providing accurate, high-quality 3D imaging of pipeline defects with high resolution and accuracy. The improvement in accuracy comes from taking into account the converted wave on the inner wall of the pipelines and the information coming from the multiple waves reflection at the bottom of the defects. Numerical and experimental results indicate that the method is effective, and that it may be potentially applied to the practical ultrasonic nondestructive testing of submarine pipelines.

Author Contributions: Conceptualization, D.P. and F.C.; methodology, D.P., X.S., F.C. and Y.Z.; software, D.P., Y.Z. and Y.T.; validation, D.P., X.S. and Y.Z.; formal analysis, D.P. and F.C.; investigation, Y.Z. and Z.F.; resources, D.P.; data curation, D.P., F.C., Y.Z. and Z.F.; writing—original draft preparation, D.P.; writing—review and editing, X.S., Y.Z. and Y.T.; visualization, D.P.; supervision, F.C.; project administration, D.P. and F.C.; funding acquisition, F.C. All authors have read and agreed to the published version of the manuscript.

Funding: This research was funded by the National Natural Science Foundation of China (No. 41704146).

Institutional Review Board Statement: Not applicable.

Informed Consent Statement: Not applicable.

Data Availability Statement: The data presented in this study are available on request from the corresponding author.

Conflicts of Interest: The authors declare no conflict of interest. The funders had no role in the design of the study; in the collection, analyses, or interpretation of data; in the writing of the manuscript, or in the decision to publish the results.

References

1. Du, F.; Li, C.; Wang, W. Development of Subsea Pipeline Buckling, Corrosion and Leakage Monitoring. *J. Mar. Sci. Eng.* **2023**, *11*, 188. [CrossRef]
2. Dong, Y.; Wang, D.; Randolph, M.F. Investigation of impact forces on pipeline by submarine landslide using material point method. *Ocean Eng.* **2017**, *146*, 21–28. [CrossRef]
3. Li, R.; Chen, B.Q.; Guedes Soares, C. Design Equation of Buckle Propagation Pressure for Pipe-in-Pipe Systems. *J. Mar. Sci. Eng.* **2023**, *11*, 622. [CrossRef]
4. Dong, Y.; Ji, G.; Fang, L.; Liu, X. Fatigue Strength Assessment of Single-Sided Girth Welds in Offshore Pipelines Subjected to Start-Up and Shut-Down Cycles. *J. Mar. Sci. Eng.* **2022**, *10*, 1879. [CrossRef]
5. Mahmutoglu, Y.; Turk, K. Received signal strength difference based leakage localization for the underwater natural gas pipelines. *Appl. Acoust.* **2019**, *153*, 14–19. [CrossRef]
6. Kakaie, A.; Soares, C.G.; Ariffin, A.K.; Punurai, W. Fatigue Reliability Analysis of Submarine Pipelines Using the Bayesian Approach. *J. Mar. Sci. Eng.* **2023**, *11*, 580. [CrossRef]
7. Dong, Y.; Liao, Z.; Wang, J.; Liu, Q.; Cui, L. Potential failure patterns of a large landslide complex in the Three Gorges Reservoir area. *Bull. Eng. Geol. Environ.* **2023**, *82*, 41. [CrossRef]
8. Hong, X.; Huang, L.; Gong, S.; Xiao, G. Shedding damage detection of metal underwater pipeline external anticorrosive coating by ultrasonic imaging based on HOG + SVM. *J. Mar. Sci. Eng.* **2021**, *9*, 364. [CrossRef]
9. Sheng, H.; Wang, P. Evaluation of Pipeline Steel Mechanical Property Distribution Based on Multimicromagnetic NDT Method. *IEEE Trans. Instrum. Meas.* **2023**, *72*, 6001715. [CrossRef]
10. Wu, D.; Liu, Z.; Wang, X.; Su, L. Composite magnetic flux leakage detection method for pipelines using alternating magnetic field excitation. *NDT E Int.* **2017**, *91*, 148–155. [CrossRef]
11. Abou-Khousa, M.A.; Rahman, M.S.U.; Donnell, K.M.; Al Qaseer, M.T. Detection of Surface Cracks in Metals using Microwave and Millimeter Wave Nondestructive Testing Techniques—A Review. *IEEE Trans. Instrum. Meas.* **2023**, *72*, 8000918. [CrossRef]
12. Yao, Y.; Tung ST, E.; Glisic, B. Crack detection and characterization techniques—An overview. *Struct. Control Health Monit.* **2014**, *21*, 1387–1413. [CrossRef]
13. Felice, M.V.; Fan, Z. Sizing of flaws using ultrasonic bulk wave testing: A review. *Ultrasonics* **2018**, *88*, 26–42. [CrossRef]
14. Vogelaar, B.; Golombok, M. Quantification and localization of internal pipe damage. *Mech. Syst. Signal Process.* **2016**, *78*, 107–117. [CrossRef]
15. Barros, B.; Conde, B.; Cabaleiro, M.; Riveiro, B. Deterministic and probabilistic-based model updating of aging steel bridges. *Structures* **2023**, *54*, 89–105. [CrossRef]
16. Morokov, E.; Levin, V.; Chernov, A.; Shanygin, A. High resolution ply-by-ply ultrasound imaging of impact damage in thick CFRP laminates by high-frequency acoustic microscopy. *Compos. Struct.* **2021**, *256*, 113102. [CrossRef]
17. Morokov, E.; Titov, S.; Levin, V. In situ high-resolution ultrasonic visualization of damage evolution in the volume of quasi-isotropic CFRP laminates under tension. *Compos. Part B Eng.* **2022**, *247*, 110360. [CrossRef]
18. Zhu, W.; Xiang, Y.; Zhang, H.; Zhang, M.; Fan, G.; Zhang, H. Super-resolution ultrasonic Lamb wave imaging based on sign coherence factor and total focusing method. *Mech. Syst. Signal Process.* **2023**, *190*, 110121. [CrossRef]
19. Drinkwater, B.W.; Wilcox, P.D. Ultrasonic arrays for non-destructive evaluation: A review. *NDT E Int.* **2006**, *39*, 525–541. [CrossRef]
20. Portzgen, N.; Gisolf, D.; Blacquiere, G. Inverse wave field extrapolation: A different NDI approach to imaging defects. *IEEE Trans. Ultrason. Ferroelectr. Freq. Control* **2006**, *54*, 118–127. [CrossRef]

21. Bai, Z.; Chen, S.; Jia, L.; Zeng, Z. Phased array ultrasonic signal compressive detection in low-pressure turbine disc. *NDT E Int.* **2017**, *89*, 1–13. [CrossRef]
22. Langenberg, K.; Berger, M.; Kreutter, T.; Mayer, K.; Schmitz, V. Synthetic aperture focusing technique signal processing. *NDT Int.* **1986**, *19*, 177–189. [CrossRef]
23. Ni, C.Y.; Chen, C.; Ying, K.N.; Dai, L.N.; Yuan, L.; Kan, W.W.; Shen, Z.H. Non-destructive laser-ultrasonic Synthetic Aperture Focusing Technique (SAFT) for 3D visualization of defects. *Photoacoustics* **2021**, *22*, 100248. [CrossRef] [PubMed]
24. Seo, H.; Pyun, D.K.; Jhang, K.Y. Synthetic aperture imaging of contact acoustic nonlinearity to visualize the closing interfaces using tone-burst ultrasonic waves. *Mech. Syst. Signal Process.* **2019**, *125*, 257–274. [CrossRef]
25. Silk, M.G. The use of diffraction-based time-of-flight measurements to locate and size defects. *Br. J. Non-Destr. Test.* **1984**, *26*, 208–213.
26. Sun, X.; Lin, L.; Jin, S. Resolution Enhancement in Ultrasonic TOFD Imaging by Combining Sparse Deconvolution and Synthetic Aperture Focusing Technique (Sparse-SAFT). *Chin. J. Mech. Eng.* **2022**, *35*, 94. [CrossRef]
27. Yang, F.; Shi, D.; Lo, L.-Y.; Mao, Q.; Zhang, J.; Lam, K.-H. Auto-Diagnosis of Time-of-Flight for Ultrasonic Signal Based on Defect Peaks Tracking Model. *Remote Sens.* **2023**, *15*, 599. [CrossRef]
28. Holmes, C.; Drinkwater, B.W.; Wilcox, P.D. Post-processing of the full matrix of ultrasonic transmit–receive array data for non-destructive evaluation. *NDT E Int.* **2005**, *38*, 701–711. [CrossRef]
29. He, H.; Sun, K.; Sun, C.; He, J.; Liang, E.; Liu, Q. Suppressing artifacts in the total focusing method using the directivity of laser ultrasound. *Photoacoustics* **2023**, *31*, 100490. [CrossRef]
30. Müller, S.; Niederleithinger, E.; Bohlen, T. Reverse time migration: A seismic imaging technique applied to synthetic ultrasonic data. *Int. J. Geophys.* **2012**, *2012*, 128465. [CrossRef]
31. He, J.; Leckey, C.A.; Leser, P.E.; Leser, W.P. Multi-mode reverse time migration damage imaging using ultrasonic guided waves. *Ultrasonics* **2019**, *94*, 319–331. [CrossRef]
32. Yang, X.; Wang, K.; Xu, Y.; Xu, L.; Hu, W.; Wang, H.; Su, Z. A reverse time migration-based multistep angular spectrum approach for ultrasonic imaging of specimens with irregular surfaces. *Ultrasonics* **2020**, *108*, 106233. [CrossRef] [PubMed]
33. Rao, J.; Wang, J.; Kollmannsberger, S.; Shi, J.; Fu, H.; Rank, E. Point cloud-based elastic reverse time migration for ultrasonic imaging of components with vertical surfaces. *Mech. Syst. Signal Process.* **2022**, *163*, 108144. [CrossRef]
34. Nguyen, L.T.; Modrak, R.T. Ultrasonic wavefield inversion and migration in complex heterogeneous structures: 2D numerical imaging and nondestructive testing experiments. *Ultrasonics* **2018**, *82*, 357–370. [CrossRef] [PubMed]
35. Whitmore, N.D. Iterative depth migration by backward time propagation. In *SEG Technical Program Expanded Abstracts 1983*; Society of Exploration Geophysicists: Houston, TX, USA, 1983; pp. 382–385. [CrossRef]
36. Baysal, E.; Kosloff, D.D.; Sherwood JW, C. Reverse time migration. *Geophysics* **1983**, *48*, 1514–1524. [CrossRef]
37. Chang, W.F.; McMechan, G.A. 3-D elastic prestack, reverse-time depth migration. *Geophysics* **1994**, *59*, 597–609. [CrossRef]
38. Ma, X.; Li, H.; Gui, Z.; Peng, X.; Li, G. Frequency-Domain Q-Compensated Reverse Time Migration Using a Stabilization Scheme. *Remote Sens.* **2022**, *14*, 5850. [CrossRef]
39. Fang, J.; Shi, Y.; Zhou, H.; Chen, H.; Zhang, Q.; Wang, N. A High-Precision Elastic Reverse-Time Migration for Complex Geologic Structure Imaging in Applied Geophysics. *Remote Sens.* **2022**, *14*, 3542. [CrossRef]
40. Fink, M. Time reversal of ultrasonic fields. I. Basic principles. *IEEE Trans. Ultrason. Ferroelectr. Freq. Control* **1992**, *39*, 555–566. [CrossRef]
41. Ji, K.; Zhao, P.; Zhuo, C.; Chen, J.; Wang, X.; Gao, S.; Fu, J. Ultrasonic full-matrix imaging of curved-surface components. *Mech. Syst. Signal Process.* **2022**, *181*, 109522. [CrossRef]
42. Liu, H.; Qi, Y.; Chen, Z.; Tong, H.; Liu, C.; Zhuang, M. Ultrasonic inspection of grouted splice sleeves in precast concrete structures using elastic reverse time migration method. *Mech. Syst. Signal Process.* **2021**, *148*, 107152. [CrossRef]
43. Zhang, Y.; Gao, X.; Zhang, J.; Jiao, J. An Ultrasonic Reverse Time Migration Imaging Method Based on Higher-Order Singular Value Decomposition. *Sensors* **2022**, *22*, 2534. [CrossRef] [PubMed]
44. Rao, J.; Saini, A.; Yang, J.; Ratassepp, M.; Fan, Z. Ultrasonic imaging of irregularly shaped notches based on elastic reverse time migration. *NDT E Int.* **2019**, *107*, 102135. [CrossRef]
45. Jia, D.; Zhang, W.; Wang, Y.; Liu, Y. A new approach for cylindrical steel structure deformation monitoring by dense point clouds. *Remote Sens.* **2021**, *13*, 2263. [CrossRef]
46. Ren, Y.; Wang, J.; Yang, Z.; Xu, X.; Chen, L. Pre-stack elastic reverse time migration in tunnels based on cylindrical coordinates. *J. Rock Mech. Geotech. Eng.* **2022**, *14*, 1933–1945. [CrossRef]
47. Zheng, Y.; Cheng, F.; Liu, J.; Fan, Z.; Han, B.; Wang, J. Elastic full-wave field simulation in 3D tunnel space with the variable staggered-grid finite-difference method in cylindrical coordinates. *J. Appl. Geophys.* **2023**, *213*, 105013. [CrossRef]
48. Nguyen, L.T.; Kocur, G.K.; Saenger, E.H. Defect mapping in pipes by ultrasonic wavefield cross-correlation: A synthetic verification. *Ultrasonics* **2018**, *90*, 153–165. [CrossRef]
49. Liu, Q.H.; Sinha, B.K. A 3D cylindrical PML/FDTD method for elastic waves in fluid-filled pressurized boreholes in triaxially stressed formations. *Geophysics* **2003**, *68*, 1731–1743. [CrossRef]
50. Virieux, J. P-SV wave propagation in heterogeneous media: Velocity-stress finite-difference method. *Geophysics* **1986**, *51*, 889–901. [CrossRef]

51. Zeng, C.; Xia, J.; Miller, R.D.; Tsoflias, G.P. An improved vacuum formulation for 2D finite-difference modeling of Rayleigh waves including surface topography and internal discontinuities. *Geophysics* **2012**, *77*, T1–T9. [CrossRef]
52. Liu, Q.H. Perfectly matched layers for elastic waves in cylindrical and spherical coordinates. *J. Acoust. Soc. Am.* **1999**, *105*, 2075–2084. [CrossRef]
53. Chattopadhyay, S.; McMechan, G.A. Imaging conditions for prestack reverse-time migration. *Geophysics* **2008**, *73*, S81–S89. [CrossRef]
54. Zhang, Y.; Sun, J. Practical issues in reverse time migration: True amplitude gathers, noise removal and harmonic source encoding. *First Break* **2009**, *27*. [CrossRef]
55. Velis, D.R.; Ulrych, T.J. Simulated annealing wavelet estimation via fourth-order cumulant matching. *Geophysics* **1996**, *61*, 1939–1948. [CrossRef]
56. Buland, A.; Omre, H. Bayesian wavelet estimation from seismic and well data. *Geophysics* **2003**, *68*, 2000–2009.